Seismic response analysis of an oil storage tank using Lagrangian fluid elements

Toshio Nagashima[*] and Takenari Tsukuda

Department of Engineering and Applied Sciences, Faculty of Science and Technology, Sophia University, 7-1 Kioicho, Chiyoda-ku, Tokyo 102-8554, Japan

Abstract.   Three-dimensional Lagrangian fluid finite element is applied to seismic response analysis of an oil storage tank with a floating roof. The fluid element utilized in the present analysis is formulated based on the displacement finite element method considering only volumetric elasticity and its element stiffness matrix is derived by using one-point integration method in order to avoid volumetric locking. The method usually adds a rotational penalty stiffness to satisfy the irrotational condition for fluid motion and modifies element mass matrices through the projected mass method to suppress spurious hourglass-mode appeared in compensation for one-point integration. In the fluid element utilized in the present paper, a small hourglass stiffness is employed. The fluid and structure domains for the objective oil storage tank are modeled by eight-node solid elements and four-node shell elements, respectively, and the transient response of the floating roof structure or the free surface are evaluated by implicit direct time integration method. The results of seismic response analyses are compared with those by other method and the validation of the present analysis using three-dimensional Lagrangian fluid finite elements is shown.

Keywords: FEM; fluid element; fluid-structure interaction; oil storage tank; seismic response

1. Introduction

The 2003 Tokachioki earthquake seriously damaged oil storage tanks with floating roofs that were located far from the seismic center. The long-period ground motion due to the earthquake induced surface oscillations of the fluid in the tanks referred to as "sloshing" and destroyed the floating roof structures of several tanks (Koketsu *et al.* 2005). In one of the tanks, the floating roof was damaged, and a fire broke out. The tank structure was completely destroyed by the fire, and the surrounding environment was also damaged. In Japan, before the earthquake, the strength of floating roof structures subjected to sloshing motion induced by the seismic motion of liquid contained in an oil storage tank had not been sufficiently investigated. Consequently, this accident led to a revision of the fire prevention laws in Japan regarding the design of oil storage tanks (Nishi *et al.* 2008a, b and 2010). Therefore, it is important to perform seismic response analyses for expected earthquake motion and to evaluate surface elevations and stress distributions of

---

*Corresponding author, Professor, E-mail: nagashim@sophia.ac.jp

floating roof structures with a view to preventing earthquake damage (Ormeno *et al*. 2012).

   The potential flow theory (Ibrahim 2005), which assumes the fluid motion to be incompressible, inviscid and irrotational, is applicable in certain engineering design problems. Linear potential analysis, in which the motion of the free surface is assumed to be small, is often valid and has satisfactory accuracy. Recently, Matsui (2007, 2009) performed sloshing analysis for a cylindrical liquid storage tank with a floating roof under seismic excitation through an analytical approach based on the potential flow theory. Moreover, Yoshida *et al*. (2008) performed fluid-structure coupling analysis for the observed wave of the 2003 Tokachioki earthquake using axisymmetric finite elements for a potential flow and an elastic floating roof structure. The authors have developed a fluid-structure strong coupling analysis system, in which the structure and fluid domains are modeled by finite elements based on Lagrange-type and Euler-type formulations, respectively, in order to perform seismic response analyses of oil storage tanks (Nagashima 2006, Nagashima *et al*. 2011).

   On the other hand, dynamic response analysis of fluid in a container using a Lagrange-type fluid finite element has been proposed (Wilson and Khalvati 1983, Chen and Taylor 1990, Calayir and Dumanoglu 1993, Dogangun *et al*. 1996, Kim and Yun 1997, Hamdan 1999, Parrinello and Borino 2007). This method models the fluid as an incompressible perfect fluid and uses continuum elements for linear elastic materials based on the displacement method, which consider only volumetric elasticity and neglects shear elasticity. In addition, the penalty stiffness for rotational motion is introduced in order to consider irrotational conditions of the fluid. Since linear elements are normally used for space discretization in the framework of the finite element method, one-point integration at the center of the element is adopted in order to derive the element stiffness matrix. Moreover, Chen and Taylor (1990) proposed the projected mass method in order to control hourglass modes that appeared in order to compensate for the one-point integration. Kim and Yun (1997) applied the Lagrange-type fluid element to two-dimensional eigenvalue and dynamic response analyses for fluid in rigid and elastic containers.

   The authors have tried to extend Kim's formulation (Kim and Yun 1997) for a fluid element, which applies one-point integration, stiffness with rotational penalty, and the projected mass method to three-dimensional problems in order to perform seismic response analyses of an oil storage tank with a floating roof. However, inappropriate deformation modes referred to as hourglass modes were still obtained for some problems. Therefore, the present paper proposes a stabilization method by adding resistance stiffness against spurious modes, which is referred to as hourglass stiffness. The magnitudes of the hourglass and rotational penalty stiffnesses are determined by a series of eigenvalue analyses for the sloshing frequency of liquid in a rigid cylindrical container, the theoretical solution of which is known, in order to search for optimized parameters. Using such parameters for the hourglass and rotational penalty stiffnesses, transient response analyses for an oil storage tank are performed. In the present analyses, the effects on the numerical results of the determination as to whether a free surface or a floating roof structure is modeled and whether the elasticity of the tank wall is considered are investigated. The response results obtained using the proposed fluid elements are compared with those obtained by potential analyses and fluid-structure strong coupling analyses using Lagrange-type solid and Euler-type fluid elements (Nagashima 2006, Nagashima *et al*. 2011).

   The remainder of the present paper is organized as follows. Section 2 presents the formulation of the Lagrange-type fluid finite elements and the analysis methods. In Section 3, the eigenvalue analyses for the sloshing motion in a rigid cylindrical tank filled with liquid are described, and the optimized range of numerical parameters for rotational penalty and hourglass control are

determined. In Section 4, the transient response analyses of a free surface or a floating roof for a single-deck type oil storage tank with a floating roof are performed by the proposed method, and the transient responses of the surface or the floating roof elevation are evaluated through comparison with various other methods. Finally, Section 5 presents a summary of the present study.

2. Analysis methods

2.1 Governing equations

The Euler equations of motion of the inviscid perfect fluid neglecting body force is defined in three-dimensional Cartesian coordinates ($i = 1, 2, 3$) as follows (Ibrahim 2005)

$$\rho_F \left(\frac{\partial v_i}{\partial t} + v_j \frac{\partial v_i}{\partial x_j} \right) = -\frac{\partial p}{\partial x_i} \tag{1}$$

where t, v_i, p, and ρ_F are the time, velocity, pressure, and mass density of the fluid, respectively.

The relation between the fluid pressure p and the volumetric strain ε_V is assumed to be as follows

$$p = -K_f \varepsilon_V \tag{2}$$

where K_f is the bulk modulus of elasticity.

The volumetric strain ε_V of the liquid can be expressed using the displacement u_i as follows

$$\varepsilon_V = \frac{\partial u_1}{\partial x_1} + \frac{\partial u_2}{\partial x_2} + \frac{\partial u_3}{\partial x_3} \tag{3}$$

Assuming a small deformation, the following equations can be approximately established.
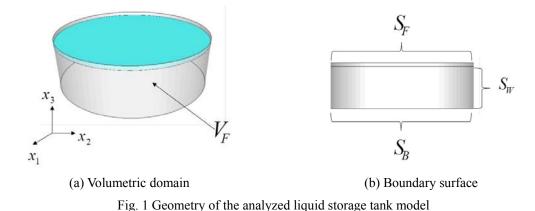
$$v_i = \frac{\partial u_i}{\partial t} \tag{4}$$

Substituting Eq. (4) into Eq. (1) and neglecting the nonlinear terms with respect to the displacement u_i, the following equation can be obtained

$$\rho_F \frac{\partial^2 u_i}{\partial t^2} = K_f \frac{\partial \varepsilon_V}{\partial x_i} \tag{5}$$

Eq. (5) is the equilibrium equation described by the displacement for a linear elastic body without a body force, neglecting the shear elasticity and considering the bulk modulus, and is referred to as Navier's equation (Fung 1965). Therefore, the inviscid perfect fluid can be described approximately as an incompressible linear elastic solid, considering only the bulk elasticity in the Lagrangian coordinate system.

In the present paper, a liquid storage container with a free surface or a floating roof, as shown in Fig. 1, where V, S_W, S_B, and S_F are the domain of the liquid, the liquid-solid interface, the bottom surface, and the free surface, respectively, is analyzed. For simplicity, the free surface is assumed

(a) Volumetric domain   (b) Boundary surface

Fig. 1 Geometry of the analyzed liquid storage tank model

to be planar, and the outward normal is assumed to point toward the x_3 direction.

The boundary condition on the free surface S_F is then described as follows

$$p = p_0 + \rho_F g u_3 \quad on \ S_F \tag{6}$$

where p_0 is the pressure at the free surface in the resting state, and g is the acceleration of gravity.

The principle of virtual work, which is equivalent to the governing equation (Eq. (5)) and the boundary condition (Eq. (6)), is described as follows

$$\iiint_V \delta\varepsilon_V K_f \varepsilon_V \, dV = -\iiint_V \delta u_i \frac{\partial^2 u_i}{\partial t^2} \, dV - \iint_{S_F} \delta u_3 \left(p_0 + \rho_F g u_3\right) dS \tag{7}$$

where the LHS, the first and the second terms of the RHS are the virtual work done by the internal force, the inertial force, and the pressure on the free surface, respectively.

If dynamic response analyses are performed under the small deformation theory without considering the initial stresses, then p_0 can, in general, be assumed to be zero. Therefore, such a condition is used in the analyses of the present paper. The LHS and the first term of the RHS of Eq. (7) relate the derivation of the stiffness matrix and the mass matrix of the fluid element. In addition, the second term of the RHS of Eq. (7) provides the derivation of the stiffness due to surface elevation.
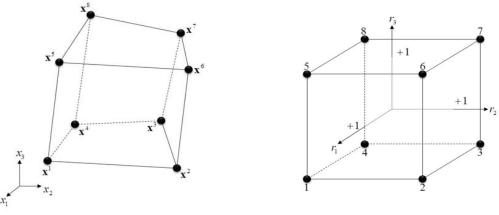
2.2 Three-dimensional eight-node hexahedral Lagrangian fluid element

The coordinates x_i ($i = 1, 2, 3$) and the displacement u_i for an eight-node hexahedral isoparametric linear element in three-dimensions, as shown in Fig. 2, can be described as follows

$$x_i = \sum_{I=1}^{8} N_I(r_1, r_2, r_3) x_i^I \tag{8}$$

$$u_i = \sum_{I=1}^{8} N_I(r_1, r_2, r_3) u_i^I \tag{9}$$

where x_i^I and u_i^I are the coordinates and the displacement at node I, respectively, r_1, r_2, and r_3 are

(a) Definition in global coordinates   (b) Definition in natural coordiates

Fig. 2 Eight-node hexahedral isoparametric linear element

the natural coordinates.

The interpolation function N_I is given as follows

$$N_I(r_1, r_2, r_3) = \frac{1}{8}\left(1 + r_1^I r_1\right)\left(1 + r_2^I r_2\right)\left(1 + r_3^I r_3\right) \tag{10}$$

where r_1^I, r_2^I, and r_3^I are the natural coordinates of r_1, r_2, and r_3, respectively, at node I.

The expressions of the approximation function and the stiffness for an eight-node hexahedral isoparametric linear element have been investigated in the field of computational solid mechanics. In particular, an explicit direct method using one-point integration has been investigated (Belytschko *et al.* 2000). Belytschko and Bindeman (1993) showed that Eq. (9) can be rewritten as follows

$$u_i = (\mathbf{a} + x_1 \mathbf{b}_1^T + x_2 \mathbf{b}_2^T + x_3 \mathbf{b}_3^T + h_1 \boldsymbol{\gamma}_1^T + h_2 \boldsymbol{\gamma}_2^T + h_3 \boldsymbol{\gamma}_3^T + h_4 \boldsymbol{\gamma}_4^T)\mathbf{u}_i \tag{11}$$

where

$$\mathbf{a} = \frac{1}{8}\left(\mathbf{s}^T - \sum_{i=1}^{3}(\mathbf{s}^T \mathbf{x}_i)\mathbf{b}_i^T\right) \tag{12.1}$$

$$\mathbf{b}_i^T = \left(\frac{\partial N_1(0,0,0)}{\partial x_i} \quad \frac{\partial N_2(0,0,0)}{\partial x_i} \quad \cdots \quad \frac{\partial N_8(0,0,0)}{\partial x_i}\right) \tag{12.2}$$

$$\mathbf{u}_i^T = \left(u_i^1 \quad u_i^2 \quad u_i^3 \quad u_i^4 \quad u_i^5 \quad u_i^6 \quad u_i^7 \quad u_i^8\right) \tag{12.3}$$

$$h_1 = r_2 r_3 \tag{13.1}$$

$$h_2 = r_1 r_3 \tag{13.2}$$

$$h_3 = r_1 r_2 \tag{13.3}$$

$$h_4 = r_1 r_2 r_3 \tag{13.4}$$

$$\boldsymbol{\gamma}_\alpha = \frac{1}{8}\left(\mathbf{h}_\alpha - \sum_{i=1}^{3}(\mathbf{h}_\alpha{}^T \mathbf{x}_i)\mathbf{b}_i \right) \quad (\alpha = 1,2,3,4) \tag{14}$$

$$\mathbf{x}_i^T = \left(x_i^1 \quad x_i^2 \quad x_i^3 \quad x_i^4 \quad x_i^5 \quad x_i^6 \quad x_i^7 \quad x_i^8 \right) \tag{15}$$

$$\mathbf{s}^T = (1 \quad 1 \quad 1 \quad 1 \quad 1 \quad 1 \quad 1 \quad 1) \tag{16.1}$$

$$\mathbf{h}_1^T = (1 \quad 1 \quad -1 \quad -1 \quad -1 \quad -1 \quad 1 \quad 1) \tag{16.2}$$

$$\mathbf{h}_2^T = (1 \quad -1 \quad -1 \quad 1 \quad -1 \quad 1 \quad 1 \quad -1) \tag{16.3}$$

$$\mathbf{h}_3^T = (1 \quad -1 \quad 1 \quad -1 \quad 1 \quad -1 \quad 1 \quad -1) \tag{16.4}$$

$$\mathbf{h}_4^T = (-1 \quad 1 \quad -1 \quad 1 \quad 1 \quad -1 \quad 1 \quad -1) \tag{16.5}$$

2.2.1 Volumetric strain stiffness

The volumetric strain defined in Eq. (3) can be described using Eq. (11), as follows

$$\varepsilon_V = \sum_{i=1}^{3} \mathbf{b}_i^T \mathbf{u}_i + \sum_{i=1}^{3} \sum_{\alpha=1}^{4} \frac{\partial h_\alpha}{\partial x_i} \boldsymbol{\gamma}_\alpha{}^T \mathbf{u}_i \tag{17}$$

Eq. (17) can be expressed as follows

$$\varepsilon_V = (\mathbf{B}_C{}^T + \mathbf{B}_{NC}{}^T)\mathbf{U} \tag{18}$$

where

$$\mathbf{B}_C{}^T = \left(\mathbf{b}_1{}^T \quad \mathbf{b}_2{}^T \quad \mathbf{b}_3{}^T \right) \tag{19.1}$$

$$\mathbf{B}_{NC}{}^T = \left(\sum_{\alpha=1}^{4} \frac{\partial h_\alpha}{\partial x_1} \boldsymbol{\gamma}_\alpha{}^T \quad \sum_{\alpha=1}^{4} \frac{\partial h_\alpha}{\partial x_2} \boldsymbol{\gamma}_\alpha{}^T \quad \sum_{\alpha=1}^{4} \frac{\partial h_\alpha}{\partial x_3} \boldsymbol{\gamma}_\alpha{}^T \right) \tag{19.2}$$

$$\mathbf{U}^T = \left(\mathbf{u}_1{}^T \quad \mathbf{u}_2{}^T \quad \mathbf{u}_3{}^T \right) \tag{19.3}$$

The LHS of Eq. (7) can be discretized by a finite element considering Eq. (18), and, consequently, the element stiffness matrix can be defined as follows

$$\mathbf{k}_V^e = K_f \mathbf{B}_C \mathbf{B}_C^T V^e + K_f \iiint_{V^e} \mathbf{B}_{NC} \mathbf{B}_{NC}^T dV \tag{20}$$

where V^e is the volume of an element.

In the derivation of Eq. (20), the following equation is used for the eight-node hexahedral isoparametric linear element

$$\iiint_{V^e} \frac{\partial h_\alpha}{\partial x_i} dV = 0 \tag{21}$$

Eq. (20) defines the element stiffness matrix using full integration. However, this element stiffness tends to provide extremely high stiffness and never produces appropriate results. This phenomenon is referred to as volumetric locking (Belytschko *et al.* 2000). Therefore, the one-point integration method is usually used to evaluate the stiffness (Wilson and Khalvati 1983, Chen and Taylor 1990, Calayir and Dumanoglu 1993, Dogangun *et al.* 1996, Kim and Yun 1997, Hamdan 1999, Parrinello and Borino 2007). However, for three-dimensional problems, the one-point integration method cannot completely eliminate spurious deformation modes. Therefore, the second term of RHS of Eq. (20) is left as a stiffness to resist spurious hourglass modes. Consequently, Eq. (20) is rewritten as follows

$$\mathbf{k}_V^e = K_f \mathbf{B}_C \mathbf{B}_C^T V^e + \alpha_{HC} K_f \iiint_{V^e} \mathbf{B}_{NC} \mathbf{B}_{NC}^T dV \tag{22}$$

where α_{HC} is a non-dimensional parameter for controlling the hourglass mode.

In Eq. (22), for the case in which α_{HC} is zero, the element stiffness can be obtained through one-point integration. On the other hand, if α_{HC} is unity, the element stiffness can be obtained through full integration. Therefore, the magnitude of hourglass stiffness can be controlled by changing the size of α_{HC}.

2.2.2 Rotational penalty stiffness

Wilson and Khalvati (1983) introduced the penalty stiffness for constraining the rotational motion of fluid in order to eliminate inappropriate rigid rotational modes. The rotation ω_i of the deformation can be defined using the displacement u_i, as follows

$$\omega_i = \frac{1}{2} e_{ijk} u_{k,j} \tag{23}$$

where e_{ijk} is the permutation symbol (Fung 1965).

Using Eq. (11), the components of rotation at the center of an element can be expressed as follows

$$\omega_1 = \frac{1}{2}(\mathbf{b}_2^T \mathbf{u}_3 - \mathbf{b}_3^T \mathbf{u}_2) = \mathbf{B}_{1\omega}^T \mathbf{U} \tag{24.1}$$

$$\omega_2 = \frac{1}{2}(\mathbf{b}_3^T \mathbf{u}_1 - \mathbf{b}_1^T \mathbf{u}_3) = \mathbf{B}_{2\omega}^T \mathbf{U} \tag{24.2}$$

$$\omega_3 = \frac{1}{2}(\mathbf{b}_1^T \mathbf{u}_2 - \mathbf{b}_2^T \mathbf{u}_1) = \mathbf{B}_{3\omega}^T \mathbf{U} \tag{24.3}$$

where

$$\mathbf{B}_{1\omega}^T = \begin{pmatrix} 0 & -\mathbf{b}_3^T/2 & \mathbf{b}_2^T/2 \end{pmatrix} \tag{25.1}$$

$$\mathbf{B}_{2\omega}^T = \begin{pmatrix} \mathbf{b}_3^T/2 & 0 & -\mathbf{b}_1^T/2 \end{pmatrix} \tag{25.2}$$

$$\mathbf{B}_{3\omega}^T = \begin{pmatrix} -\mathbf{b}_2^T/2 & \mathbf{b}_1^T/2 & 0 \end{pmatrix} \tag{25.3}$$

Consequently, the penalty stiffness matrix for rotational motion is defined as follows

$$\mathbf{k}_{RP}{}^e = \alpha_{RP} K_f (\mathbf{B}_{1\omega} \mathbf{B}_{1\omega}^T + \mathbf{B}_{2\omega} \mathbf{B}_{2\omega}^T + \mathbf{B}_{3\omega} \mathbf{B}_{3\omega}^T) V^e \tag{26}$$

where α_{RP} is non-dimensional parameter for controlling the effect of the penalty stiffness.

2.2.3 Element stiffness matrix

As described above, the element stiffness matrix used in the present analyses is defined as follows

$$\mathbf{k}^e = K_f \mathbf{b}_C \mathbf{b}_C^T V^e + \alpha_{RP} \left(\mathbf{b}_{1\omega} \mathbf{b}_{1\omega}^T + \mathbf{b}_{2\omega} \mathbf{b}_{2\omega}^T + \mathbf{b}_{3\omega} \mathbf{b}_{3\omega}^T \right) V^e + \alpha_{HC} K_f \iiint_{V^e} \mathbf{b}_{NC} \mathbf{b}_{NC}^T dV \tag{27}$$

The first term of the RHS of Eq. (27) is the stiffness term obtained by one-point integration at the center of an element. The second term is the rotational penalty term, and the third term is the additional term for controlling hourglass modes. Gauss numerical integration using $2 \times 2 \times 2$ points is used for the volumetric integration of the third term. In addition, the optimum values of α_{RP} and α_{HC} are determined through preliminary analyses.

2.2.4 Element mass matrix

The mass matrix for the fluid element can be obtained by discretizing the first term of the RHS of Eq. (7). Specifically, the mass matrix is defined by the Gauss numerical integration using $2 \times 2 \times 2$ points, as in conventional displacement-based FEM, as follows

$$\mathbf{m}^e = \rho_F \iiint_{V^e} \mathbf{N}^T \mathbf{N} dV \tag{28}$$

where

$$\mathbf{N} = \begin{bmatrix} N_1(r_1, r_2, r_3) & 0 & 0 & \cdots & 0 \\ 0 & N_1(r_1, r_2, r_3) & 0 & \cdots & 0 \\ 0 & 0 & N_1(r_1, r_2, r_3) & \cdots & N_8(r_1, r_2, r_3) \end{bmatrix} \tag{29}$$

On the other hand, as is obvious from Eq. (11), the element has 12 dependent hourglass modes, which are constructed of four modes in each axial direction x_i. The modes can be expressed by the nodal displacement at an element as follows

$$\mathbf{g}_{1\alpha}^T = \begin{pmatrix} \mathbf{h}_\alpha^T & \mathbf{0} & \mathbf{0} \end{pmatrix} \tag{30.1}$$

$$\mathbf{g}_{2\alpha}^T = \begin{pmatrix} \mathbf{0} & \mathbf{h}_\alpha^T & \mathbf{0} \end{pmatrix} \tag{30.2}$$

$$\mathbf{g}_{3\alpha}^T = \begin{pmatrix} \mathbf{0} & \mathbf{0} & \mathbf{h}_\alpha^T \end{pmatrix} \tag{30.3}$$

Chen and Taylor (1990) proposed the projected mass method to eliminate emerged hourglass modes in compensation for one-point integration and modified the mass matrix for a two-dimensional fluid element. In the present study, this method is extended to three-dimensional problems. Specifically, instead of using Eq. (28), the mass matrix for the fluid element is redefined as follows

$$\mathbf{m}_{MP}^{\ e} = \mathbf{Q}^T \mathbf{m}^e \mathbf{Q} \tag{31}$$

where

$$\mathbf{Q} = \mathbf{I}_{24} - \frac{1}{8} \sum_{\alpha=1}^{4} (\mathbf{g}_{1\alpha} \mathbf{g}_{1\alpha}^T + \mathbf{g}_{2\alpha} \mathbf{g}_{2\alpha}^T + \mathbf{g}_{3\alpha} \mathbf{g}_{3\alpha}^T) \tag{32}$$

and $\mathbf{I}_{24}$ is the unit matrix with 24 rows and 24 columns.

In fact, as shown in following equations, it can be shown that the product of matrix Q and the hourglass modes $\mathbf{g}_{1\beta}$, $\mathbf{g}_{2\beta}$, and $\mathbf{g}_{3\beta}$ are zero vectors

$$\mathbf{Qg}_{1\beta} = \mathbf{g}_{1\beta} - \frac{1}{8}\sum_{\beta=1}^{4}(\mathbf{g}_{1\alpha}\mathbf{g}_{1\alpha}^T + \mathbf{g}_{2\alpha}\mathbf{g}_{2\alpha}^T + \mathbf{g}_{3\alpha}\mathbf{g}_{3\alpha}^T)\mathbf{g}_{1\beta} = \mathbf{g}_{1\beta} - \frac{1}{8}\mathbf{g}_{1\beta}(\mathbf{g}_{1\beta}^T\mathbf{g}_{1\beta}) = \mathbf{0} \tag{33.1}$$

$$\mathbf{Qg}_{2\beta} = \mathbf{g}_{2\beta} - \frac{1}{8}\sum_{\beta=1}^{4}(\mathbf{g}_{1\alpha}\mathbf{g}_{1\alpha}^T + \mathbf{g}_{2\alpha}\mathbf{g}_{2\alpha}^T + \mathbf{g}_{3\alpha}\mathbf{g}_{3\alpha}^T)\mathbf{g}_{2\beta} = \mathbf{g}_{2\beta} - \frac{1}{8}\mathbf{g}_{2\beta}(\mathbf{g}_{2\beta}^T\mathbf{g}_{2\beta}) = \mathbf{0} \tag{33.2}$$

$$\mathbf{Qg}_{3\beta} = \mathbf{g}_{3\beta} - \frac{1}{8}\sum_{\beta=1}^{4}(\mathbf{g}_{1\alpha}\mathbf{g}_{1\alpha}^T + \mathbf{g}_{2\alpha}\mathbf{g}_{2\alpha}^T + \mathbf{g}_{3\alpha}\mathbf{g}_{3\alpha}^T)\mathbf{g}_{3\beta} = \mathbf{g}_{3\beta} - \frac{1}{8}\mathbf{g}_{3\beta}(\mathbf{g}_{3\beta}^T\mathbf{g}_{3\beta}) = \mathbf{0} \tag{33.3}$$

Therefore, if the mass matrix defined by Eq. (31) is used, the product of the mass matrix and the hourglass modes is a zero vector, and so the mass matrix does not affect the hourglass modes. Consequently, the appearance of hourglass modes is expected to be suppressed.

2.3. Treatment for free surface

If an eight-node hexahedral linear fluid element is used, the face of the element corresponding to the free surface becomes a quadrilateral. Therefore, the stiffness matrix on the movement of the free surface against gravity in the x_3 direction can be obtained by discretizing the second term of the RHS of Eq. (7) using four-node quadrilateral elements as follows

$$\mathbf{k}_S^e = \rho_F g \iint_{S^e} \mathbf{N}_3\mathbf{N}_3^T dS \tag{34}$$

where

$$\mathbf{N}_3^T = \begin{bmatrix} 0 & 0 & N_1(r_1,r_2,1) & \cdots & N_8(r_1,r_2,1) \end{bmatrix} \tag{35}$$

3. Sloshing natural frequency analysis of a liquid in the rigid cylindrical tank

The sloshing natural frequency analyses of the cylindrical rigid tank with a free surface, a diameter of 80 m, and a liquid level of 20 m are performed using the Lagrangian fluid finite elements proposed in the present study. The dimensions of the tank correspond to an oil storage tank with a floating roof, the analysis of which will be described later herein. In the analysis, the fluid domain is divided into eight-node hexahedral solid elements and the free surface is modeled by four-node quadrilateral shell elements. The finite element model used in the present analysis is shown in Fig. 3. In the model, the displacement components normal to the bottom and wall surfaces of the tank are constrained in order to consider the slip conditions between the contained fluid and the rigid tank. Undamped eigenvalue analyses were performed by varying the rotational penalty parameters α_{RP} between 10^{-4} and 10^2 and the hourglass control parameters α_{HC} between 10^{-9} and 10^{-3} in order to investigate the optimal values of the parameters and the effect of the projected mass method, and the obtained results were compared with the exact values given by the potential theory. In the present analysis, the contained liquid is assumed to be water, the bulk modulus and the density of which are 2.19 GPa and 1,000 kg/m^3, respectively, and the acceleration of gravity is assumed to be 9.80665 m/s^2.

Toshio Nagashima and Takenari Tsukuda

Table 1 Natural frequencies for various α_{RP} and α_{HC} obtained without using the projected mass method (unit: Hz)

α_{RP}	α_{HC}	(1,1) mode	(2,1) mode	(0,1) mode	(3,1) mode	(4,1) mode	(1,2) mode
1.0×10^{-4}	0	0.0*	0.0*	0.0*	0.0*	0.0*	0.0*
1.0×10^{-3}	0	0.0*	0.0*	0.0*	0.0*	0.0*	0.0*
1.0×10^{-2}	0	0.0*	0.0*	0.0*	0.0*	0.0*	0.0*
1.0×10^{-1}	0	0.0*	0.0*	0.0*	0.0*	0.0*	0.0*
1	0	0.0*	0.0*	0.0*	0.0*	0.0*	0.0*
10	0	0.0*	0.0*	0.0*	0.0*	0.0*	0.0*
100	0	0.0*	0.0*	0.0*	0.0*	0.0*	0.0*
1.0×10^{-4}	1.0×10^{-9}	0.00117*	0.00354*	0.00560*	0.00600*	0.00728*	0.00774*
1.0×10^{-3}	1.0×10^{-9}	0.00117*	0.00354*	0.00600*	0.00635*	0.00728*	0.00774*
1.0×10^{-2}	1.0×10^{-9}	0.00117*	0.00354*	0.00600*	0.00650*	0.00728*	0.00774*
1.0×10^{-1}	1.0×10^{-9}	0.00117*	0.00354*	0.00600*	0.00652*	0.00728*	0.00774*
1	1.0×10^{-9}	0.00117*	0.00354*	0.00600*	0.00653*	0.00728*	0.00774*
10	1.0×10^{-9}	0.00117*	0.00354*	0.00600*	0.00655*	0.00728*	0.00774*
100	1.0×10^{-9}	0.00117*	0.00354*	0.00600*	0.00658*	0.00728*	0.00774*
1.0×10^{-4}	1.0×10^{-8}	0.00370*	0.01120*	0.01504*	0.01897*	0.02129*	0.02362*
1.0×10^{-3}	1.0×10^{-8}	0.00370*	0.01120*	0.01540*	0.01897*	0.02302*	0.02449*
1.0×10^{-2}	1.0×10^{-8}	0.00370*	0.01120*	0.01594*	0.01897*	0.02302*	0.02449*
1.0×10^{-1}	1.0×10^{-8}	0.00370*	0.01120*	0.01608*	0.01897*	0.02302*	0.02449*
1	1.0×10^{-8}	0.00370*	0.01120*	0.01613*	0.01897*	0.02302*	0.02449*
10	1.0×10^{-8}	0.00370*	0.01120*	0.01619*	0.01897*	0.02302*	0.02449*
100	1.0×10^{-8}	0.00370*	0.01120*	0.01630*	0.01897*	0.02302*	0.02449*
1.0×10^{-4}	1.0×10^{-6}	0.03663*	0.07347*	0.09114 ×	0.11076*	0.11294#	0.13139 ×
1.0×10^{-3}	1.0×10^{-6}	0.03663*	0.09114 ×	0.11076*	0.11505*	0.13141 ×	0.15107 ×
1.0×10^{-2}	1.0×10^{-6}	0.03663*	0.09114 ×	0.11076*	0.11584*	0.13141 ×	0.15107 ×
1.0×10^{-1}	1.0×10^{-6}	0.03663*	0.09114 ×	0.11076*	0.11666*	0.13142 ×	0.15107 ×
1	1.0×10^{-6}	0.03663*	0.09114 ×	0.11076*	0.11704*	0.13170 ×	0.15108 ×
10	1.0×10^{-6}	0.03663*	0.09114 ×	0.11076*	0.11704*	0.13170 ×	0.15108 ×
100	1.0×10^{-6}	0.03663*	0.09118 ×	0.11076*	0.11721*	0.13413 ×	0.15117 ×
1.0×10^{-4}	1.0×10^{-3}	0.07103#	0.09151 ×	0.11338#	0.13297 ×	0.15278 ×	0.15320#
1.0×10^{-3}	1.0×10^{-3}	**0.09129**	**0.13300**	**0.15284**	**0.16380**	0.18579 ×	0.19266 ×
1.0×10^{-2}	1.0×10^{-3}	**0.09129**	**0.13300**	**0.15285**	**0.16383**	0.18583 ×	0.19279 ×
1.0×10^{-1}	1.0×10^{-3}	**0.09129**	**0.13301**	**0.15285**	**0.16385**	0.18585 ×	0.19289 ×
1	1.0×10^{-3}	**0.09129**	**0.13304**	**0.15285**	**0.16406**	0.18602 ×	0.19366 ×
10	1.0×10^{-3}	**0.09129**	**0.13324**	**0.15287**	**0.16594**	0.18739 ×	0.20025 ×
100	1.0×10^{-3}	**0.09134**	**0.13423**	**0.15296**	0.17951 ×	0.19709 ×	0.22893 ×
Theory		0.09112	0.13137	0.15095	0.15912	0.18083	0.18108

Table 2 Natural frequencies for various α_{RP} and α_{HC} obtained using the projected mass method (unit: Hz)

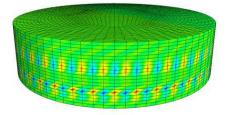| α_{RP}	α_{HC}	(1,1) mode	(2,1) mode	(0,1) mode	(3,1) mode	(4,1) mode	(1,2) mode
1.0×10^{-4}	0	0.0*	0.0*	-	0.0*	0.0*	-
1.0×10^{-3}	0	0.0*	-	-	0.0*	-	0.0*
1.0×10^{-2}	0	-	-	-	0.0*	-	0.0*
1.0×10^{-1}	0	0.0*	0.0*	0.0*	0.0*	0.0*	-
1	0	-	0.0*	0.0*	0.0*	-	-
10	0	-	-	-	0.0*	0.0*	-
100	0	0.0*	-	-	0.0*	-	0.0*
1.0×10^{-4}	1.0×10^{-9}	0.07085#	0.07705*	0.08451*	0.09091*	0.09114	0.10897*
1.0×10^{-3}	1.0×10^{-9}	0.07610*	0.09114 ×	0.10589*	0.13139 ×	0.13508*	0.15888*
1.0×10^{-2}	1.0×10^{-9}	0.07610*	0.09114 ×	0.13141 ×	0.13807*	0.15892*	0.15922 ×
1.0×10^{-1}	1.0×10^{-9}	0.07610*	0.09114 ×	0.13141 ×	0.15107 ×	0.15892*	0.15924 ×
1	1.0×10^{-9}	0.07610*	0.09114 ×	0.13142 ×	0.15107 ×	0.15892*	0.15943 ×
10	1.0×10^{-9}	0.07610*	0.09114 ×	0.13169 ×	0.15108 ×	0.15892*	0.16125 ×
100	1.0×10^{-9}	0.07610*	0.09118 ×	0.13412 ×	0.15116 ×	0.15892*	0.17398 ×
1.0×10^{-4}	1.0×10^{-8}	0.07085#	0.09114	0.11294 #	0.13139	0.15107	0.15147#
1.0×10^{-3}	1.0×10^{-8}	**0.09114**	**0.13139**	**0.15107**	**0.15922**	**0.18109**	**0.18124**
1.0×10^{-2}	1.0×10^{-8}	**0.09114**	**0.13139**	**0.15107**	**0.15922**	**0.18110**	**0.18124**
1.0×10^{-1}	1.0×10^{-8}	**0.09114**	**0.13139**	**0.15107**	**0.15924**	**0.18118**	**0.18126**
1	1.0×10^{-8}	**0.09114**	**0.13142**	**0.15107**	**0.15943**	0.18140	0.18192
10	1.0×10^{-8}	**0.09114**	**0.13153**	**0.15108**	**0.16125**	0.18268	0.18813
100	1.0×10^{-8}	**0.09118**	**0.13248**	**0.15116**	0.17398	0.19203	0.21482
1.0×10^{-4}	1.0×10^{-6}	0.07085#	0.09114 ×	0.11294#	0.13139 ×	0.15107 ×	0.15147#
1.0×10^{-3}	1.0×10^{-6}	**0.09114**	**0.13139**	**0.15107**	**0.15922**	**0.18110**	**0.18124**
1.0×10^{-2}	1.0×10^{-6}	**0.09114**	**0.13139**	**0.15107**	**0.15922**	**0.18111**	**0.18124**
1.0×10^{-1}	1.0×10^{-6}	**0.09114**	**0.13139**	**0.15107**	**0.15924**	**0.18119**	**0.18126**
1	1.0×10^{-6}	**0.09114**	**0.13142**	**0.15107**	**0.15944**	0.18141 ×	0.18193 ×
10	1.0×10^{-6}	**0.09114**	**0.13153**	**0.15108**	**0.16125**	0.18269 ×	0.18814 ×
100	1.0×10^{-6}	**0.09118**	**0.13249**	**0.15117**	0.17399 ×	0.19204 ×	0.21485 ×
1.0×10^{-4}	1.0×10^{-3}	0.07103#	0.09151 ×	0.11338#	0.13297 ×	0.15278 ×	0.15320#
1.0×10^{-3}	1.0×10^{-3}	**0.09129**	**0.13300**	**0.15284**	**0.16380**	0.18579 ×	0.19266 ×
1.0×10^{-2}	1.0×10^{-3}	**0.09129**	**0.13300**	**0.15285**	**0.16383**	0.18583 ×	0.19279 ×
1.0×10^{-1}	1.0×10^{-3}	**0.09129**	**0.13301**	**0.15285**	**0.16385**	0.18585 ×	0.19289 ×
1	1.0×10^{-3}	**0.09129**	**0.13304**	**0.15285**	**0.16406**	0.18602 ×	0.19366 ×
10	1.0×10^{-3}	**0.09129**	**0.13324**	**0.15287**	**0.16594**	0.18740 ×	0.20025 ×
100	1.0×10^{-3}	**0.09134**	**0.13423**	**0.15296**	0.17951 ×	0.19710 ×	0.22894 ×
Theory		0.09112	0.13137	0.15095	0.15912	0.18083	0.18108

Number of nodes : 36,141
Number of hexahedron elements : 33,600
Number of quadrilateral elements : 1,680

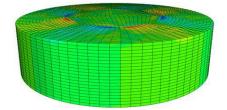Fig. 3 Finite element model of the liquid in the cylindrical tank

First, the eigenvalue analyses of the sloshing natural frequency were performed without the projected mass method by changing the rotational penalty parameter α_{RP} and the hourglass control parameters α_{HC}, and the obtained results are summarized in Table 1, where the obtained natural frequencies are given in terms of the circumferential wave number n and the radial wave number m. For example, (1,1) and (1,2) indicate the first and second sloshing modes, respectively. Second, analyses using the projected mass method were performed, and the results are summarized in Table 2. In Tables 1 and 2, the "*" and "#" symbols indicate the occurrence of hourglass and rigid rotational modes, respectively. In addition the "-" symbol indicates the impossibility of analysis, and the "x" symbol indicates that improper eigenmodes were obtained. On the other hand, the numerical values highlighted in boldface type indicate natural frequencies for which the eigenvalues and eigenmodes are acceptable when compared with theoretical values. Typical spurious hourglass and rigid rotational modes are shown in Fig. 4. The (1,1) modes in cases of α_{RP} $= 10^{-3}$ and $\alpha_{HC} = 10^{-12}$, and $\alpha_{RP} = 10^{-4}$ and $\alpha_{HC} = 10^{-6}$ are shown in Figs. 4(a) and (b), respectively,

Table 3 Appropriate natural frequencies obtained using the projected mass method (unit: Hz)

α_{RP}	α_{HC}	(1,1) mode	(2,1) mode	(0,1) mode	(3,1) mode	(4,1) mode	(1,2) mode
1.0×10^{-3}	1.0×10^{-8}	0.091135	0.13139	0.15107	0.15922	0.18109	0.18124
		(0.014%)	(0.014%)	(0.080%)	(0.061%)	(0.142%)	(0.088%)
1.0×10^{-2}	1.0×10^{-8}	0.091135	0.13139	0.15107	0.15922	0.18110	0.18124
		(0.014%)	(0.014%)	(0.080%)	(0.061%)	(0.148%)	(0.088%)
1.0×10^{-1}	1.0×10^{-8}	0.091135	0.13139	0.15107	0.15924	0.18118	0.18126
		(0.014%)	(0.014%)	(0.080%)	(0.074%)	(0.192%)	(0.099%)
1.0×10^{-3}	1.0×10^{-6}	0.091135	0.13139	0.15107	0.15922	0.18110	0.18124
		(0.014%)	(0.014%)	(0.080%)	(0.061%)	(0.148%)	(0.088%)
1.0×10^{-2}	1.0×10^{-6}	0.091135	0.13139	0.15107	0.15922	0.18111	0.18124
		(0.014%)	(0.014%)	(0.080%)	(0.061%)	(0.153%)	(0.088%)
1.0×10^{-1}	1.0×10^{-6}	0.091136	0.13139	0.15107	0.15924	0.18119	0.18126
		(0.015%)	(0.014%)	(0.080%)	(0.074%)	(0.197%)	(0.099%)
Theory		0.091122	0.13137	0.15095	0.15912	0.18083	0.18108

(a) Hourglass mode obtained for $\alpha_{RP} = 10^{-3}$ and $\alpha_{HC} = 10^{-12}$ using the projected mass method

(b) Rotational mode obtained for $\alpha_{RP} = 10^{-4}$ and $\alpha_{HC} = 10^{-6}$ using the project mass method
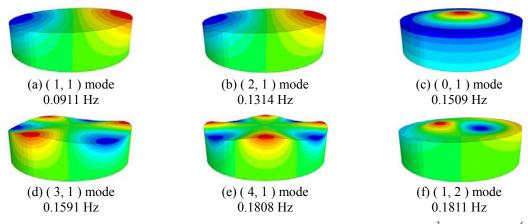
Fig. 4 Typical spurious eigenmodes

(a) (1, 1) mode
0.0911 Hz

(b) (2, 1) mode
0.1314 Hz

(c) (0, 1) mode
0.1509 Hz

(d) (3, 1) mode
0.1591 Hz

(e) (4, 1) mode
0.1808 Hz

(f) (1, 2) mode
0.1811 Hz

Fig. 5 Eigenmodes of the liquid in the cylindrical tank obtained for $\alpha_{RP} = 10^{-3}$ and $\alpha_{HC} = 10^{-6}$ using the projected mass method

and both cases were computed using the projected mass method. Table 3 shows that appropriate results were obtained by using the projected mass method and setting α_{RP} to a value between 10^{-3} and 10^{-1} and α_{HC} to a value between 10^{-8} and 10^{-6}. Table 3 summarizes the appropriately obtained results, which agree with the theoretical results. Typical appropriate first and second sloshing eigenmodes obtained using the projected mass method and setting α_{RP} and α_{HC} to 10^{-3} and 10^{-6}, respectively, are shown in Fig. 5. Therefore, in the subsequent analyses, the projected mass method is used, and α_{RP} and α_{HC} are taken as 10^{-3} and 10^{-6}, respectively.

4. Seismic response analysis of an oil storage tank with a floating roof

4.1 Tank geometry

Sloshing eigenvalue and transient seismic response analyses were performed for a 100,000 kiloliter class government-stockpiled oil storage tank with a single-deck floating roof. This storage tank has a diameter of 80 m, a height of 25 m, a liquid level of 20 m, a bottom thickness of 9 mm,
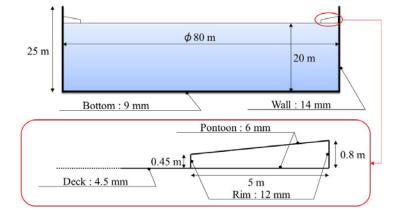
Fig. 6 Dimensions of the oil storage tank with a floating roof analyzed in the present study

and a wall thickness of 14 mm, as shown in Fig. 6. Although the thickness of the lowest part of the tank wall is usually around 32 mm in the actual 80 m-diameter class oil storage tank, the wall of the model in the present analysis has a constant thickness of 14 mm, which is the averaged thickness in height direction. However, the actual distribution of the wall thickness is supposed to provide almost the same results because the maximum surface elevations are insensitive to the wall stiffness in the analysis as shown later. The structure of a roof having floats called pontoon was also considered. The Young's modulus, Poisson's ratio, and mass density of both the tank and roof structures were assumed to be 200 GPa, 0.3, and 8,000 kg/m^3, respectively, and the properties of the liquid contained in the tank were as described in Section 3.

4.2 Analysis cases

First, undamped sloshing eigenvalue analyses of the liquid in the tank were performed. In these analyses, the effects of the methods used to model the tank wall and the floating roof on the numerical results were investigated. In addition, for comparison, analyses using an Euler-type fluid element based on the potential flow theory (Nagashima 2006, Nagashima *et al*. 2011) were also performed. The analysis cases are summarized in Table 4. Case E3 in Table 4, for example, corresponds to the undamped sloshing eigenvalue analysis of liquid in the tank with a free surface while considering the elasticity of the tank wall modeled by Lagrangian fluid finite elements.

Second, transient response analyses using the published acceleration data HKD129EW, which is provided by K-NET (http://www.k-net.bosai.go.jp/) of the National Research Institute for Earth Science and Disaster Prevention (NIED) of Japan, were performed. In addition to the eigenvalue analyses, the effects of the modeling methods on the numerical results were examined. The analysis cases for the transient response analyses are summarized in Table 5. Case T7 in Table 5, for example, corresponds to the transient response analysis of liquid in the tank with a floating roof while considering the elasticity of the tank wall modeled by the Lagrangian fluid finite elements.
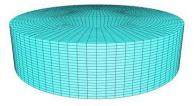
4.3 Finite element model

The liquid domain in the tank was divided into eight-node hexahedral solid elements, and when

Table 4 Cases for natural sloshing frequency analyses

Case	Fluid element type	Tank wall	Floating roof or free surface
E1	Euler	Rigid	Free surface
E2	Langrange	Rigid	Free surface
E3	Langrange	Elastic	Free surface
E4	Langrange	Rigid	Floating roof
E5	Langrange	Elastic	Floating roof

Table 5 Cases for transient response analyses

Case	Fluid element type	Tank wall	Floating roof or free surface	Remarks
T1	Euler	Rigid	Free surface	Using linear potential flow theory
T2	Euler	Elastic	Free surface	Strong-coupling (Euler/Langrange)
T3	Euler	Elastic	Floating roof	Strong-coupling (Euler/Langrange)
T4	Euler	Rigid	Floating roof	Strong-coupling (Euler/Langrange)
T5	Langrange	Rigid	Free surface	Using the proposed fluid elemtents
T6	Langrange	Elastic	Free surface	Using the proposed fluid elemtents
T7	Langrange	Elastic	Floating roof	Using the proposed fluid elemtents
T8	Langrange	Rigid	Floating roof	Using the proposed fluid elemtents

(a) Fluid
Number of nodes : 36,141
Number of elements : 33,600

(b) Fluid surface
Number of nodes :1,721
Number of elements : 1,680

(c) Wall
Number of nodes : 2,080
Number of elements : 2,000

(d) Pontoon roof
Number of nodes : 2,281
Number of elements : 2,320

Fig. 7 Finite element models of the tank structures and the liquid

the Lagrangian fluid elements were used, four-node quadrilateral fluid shell elements were placed at the liquid level. In addition, the tank structures, such as the tank wall and the floating roof, were modeled by four-node quadrilateral structure shell elements. The finite element models for the contained liquid, the liquid surface, the tank wall, and the floating roof are shown in Figs. 7(a) through 7(d), respectively. For example, Case E1 uses the finite element model shown in Fig. 7(a), and Cases E2, E3, E4, and E5 use this finite element model in conjunction with the finite element models shown in Figs. 7(b) through 7(d) based on the analysis conditions.

4.4 Constraint conditions

The displacement component in the x_3 direction u_3 of the node for the fluid element is constrained on the tank bottom S_B, whereas the displacement of the nodes for solid elements isperfectly constrained. When the tank wall is assumed to be rigid, the displacement component un normal to the interface between the tank wall and the liquid is constrained for the nodes of the fluid elements. When the elasticity of the tank wall is considered, the constraint conditions with respect to the displacement components of the outward normal u_n^F and u_n^W for the fluid and solid elements, as shown in Fig. 8(a), are given as follows
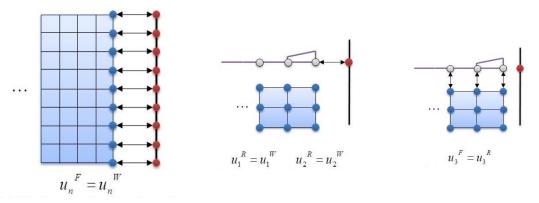
$$u_n^F = u_n^W \tag{36}$$

Regarding the nodes located on the outer edge of the floating roof model, when the tank wall is assumed to be rigid, the displacement components in the horizontal plane u_1^R and u_2^R are constrained as follows

$$u_1^R = u_2^R = 0 \tag{37}$$

On the other hand, when the elasticity of the tank wall is considered, as shown in Figs. 8(b) and (c), the constraint conditions between the nodes on the tank structure and the nodes on the floating roof and those between the nodes on the liquid and the nodes on the floating roof are given as follows

$$u_1^R = u_1^W, u_2^R = u_2^W, u_3^R = u_3^W \tag{38}$$

(a) Between the fluid and the wall   (b) Between the roof and the wall (c) Between the fluid and the roof

Fig. 8 Constraint conditions between the fluid and various structures

4.5 Results and discussion

First, undamped sloshing eigenvalue analyses were performed, and the results were compared with the theoretical solutions, as shown in Table 6. The results for Cases E1 through E4 were similar, and the differences between the numerical results and the exact solutions for the first and second sloshing modes were less than 0.5%. The results for these cases are almost identical. The first and the second sloshing modes obtained for Case E2 are shown in Fig. 9.

Second, the transient response analyses were performed by enforcing the horizontal acceleration wave, which is shown in Fig. 10, to the tank model. A Rayleigh damping of 0.5%, corresponding to the first sloshing mode, was assumed. In addition, the time increment is set to 0.01 seconds, and computation was performed for 290 seconds using 29,000 steps. As shown in Fig. 11, the evaluation point is located along the circular edge, farthest from the tank axis. The

Table 6 Obtained natural frequencies for the first and second sloshing modes

Case	1st sloshing mode		2nd sloshing mode	
	Frequency [Hz]	Error	Frequency [Hz]	Error
E1	0.09111	0.012%	0.18067	0.226%
E2	0.09114	0.014%	0.18124	0.088%
E3	0.09086	0.283%	0.18112	0.022%
E4	0.09106	0.072%	0.18064	0.243%
E5	0.09079	0.364%	0.18054	0.298%
Theory	0.09112		0.18108	

(a) 1st sloshing mode
0.09112 Hz

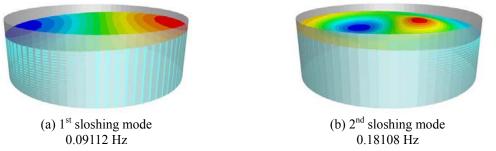(b) 2nd sloshing mode
0.18108 Hz

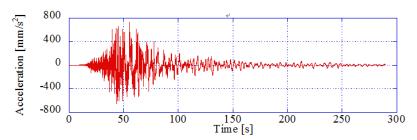Fig. 9 First and second sloshing modes obtained by eigenvalue analyses for Case E2

Fig. 10 Observed seismic acceleration provided by K-NET (HKD129EW)
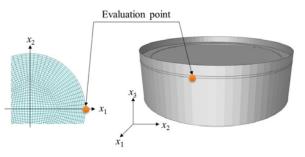
Fig. 11 Evaluation point for the transient analyses

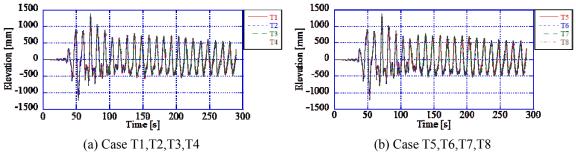| (a) Case T1,T2,T3,T4 | (b) Case T5,T6,T7,T8 |

Fig. 12 Transient responses of surface elevation obtained using Euler-type fluid elements

displacement components u_3 in the perpendicular direction for Cases T1 through T4 and Cases T5 through T8 are shown in Fig. 12. In addition, in order to compare the results obtained using the proposed Lagrangian element and the results obtained by the Eulerian element, the displacement components u_3 in the perpendicular direction during the period from 50 to 100 seconds for Cases T1, T2, T5, and T6 and Cases T3, T4, T7, and T8 are shown in Fig. 13. Moreover, the maximum elevation is summarized in Table 7. As shown in Fig. 12, and Table 7, the transient response of surface elevation was almost identical for all cases. In addition, the analysis results obtained using the Lagrangian fluid element agreed well with the results obtained using the linear potential flow theory and the strong coupling method between the Eulerian fluid element and the Lagrangian structural element (Nagashima 2006, Nagashima *et al*. 2011). Consequently, the dynamic response analyses of the tank are almost independent of the tank wall elasticity, and so the elastic effect of the tank on the response is small. Furthermore, the maximum elevation of the floating roof is almost the same as that obtained using the free surface. However, Cases T4 and T8, which model the floating roof directly, are preferable because stress evaluation of the roof is required. In the present analyses, although the second order sloshing mode would appear dominantly in the case of the transient seismic analysis of 80 m-diameter class tank using HKD129EW, a Rayleigh damping of 0.5%, corresponding to only the first sloshing mode, is employed. Therefore, a Rayleigh damping regarding the second sloshing mode should be considered. In addition, the results for the transient analyses summarized in Table 7 show that the maximum displacement of the floating roof is greater than that of the free surface. These results may not be qualitatively-correct. The cause could be due to the fact that both the floating roof and free surface models use the same Rayleigh damping of 0.5%. In order to improve the accuracy of transient analyses, thoughtful consideration for the damping factor should be given. This is an issue in the future.
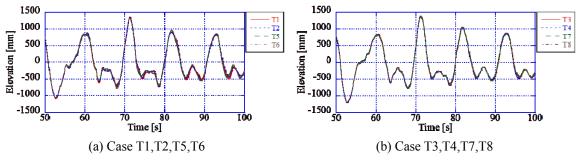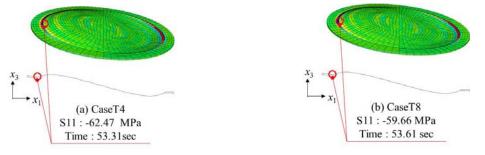
(a) Case T1,T2,T5,T6   (b) Case T3,T4,T7,T8

Fig. 13 Transient responses of surface elevation during 50-100 seconds

Table 7 Maximum surface elevations obtained by Case T1 through Case T8

Case	Max displacement	
	mm	s
T1	1321.059	71.31
T2	1338.739	71.32
T3	1379.725	71.28
T4	1362.874	71.25
T5	1313.600	71.29
T6	1352.000	71.29
T7	1380.400	71.29
T8	1345.200	71.29

(a) CaseT4
S11 : -62.47 MPa
Time : 53.31sec

(b) CaseT8
S11 : -59.66 MPa
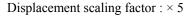Time : 53.61 sec

Displacement scaling factor : × 5

Fig. 14 Bending stress distribution of the floating roof

The bending stress distributions of the floating roof obtained for Cases T4 and T8 are shown in Fig. 14, where the normal stress in the x_1 direction is evaluated as the bending stress. The results are similar for both cases and provide the maximum bending stresses at the junctional region between the pontoon and the deck.

In addition, the computation time and the memory required to solve the system equations for the eight analysis cases, as well as the computational environments, are listed in Table 8. Although the number of degrees of freedom of a node for an Eulerian element is one, that for a

Table 8 Computation time and required memory for Case T1 through Case T8

Case	Number of DOFs	CPU time*		Required memory for non-zero terms (PARDISO/IMKL)	
T1	36,141	95.2	min	13,036,817	<99 MB>
T2	48,621	146.8	min	38,779,713	<296 MB>
T3	72,153	223.3	min	60,901,633	<465 MB>
T4	49,927	153.0	min	40,822,767	<311 MB>
T5	108,423	668.7	min	109,635,205	<836 MB>
T6	120,903	805.6	min	125,277,839	<956 MB>
T7	144,435	901.7	min	143,018,173	<1091 MB>
T8	122,109	784.8	min	125,277,647	<956 MB>

*Quad-Core Xeon 2.66 GHz (X5550), two-CPUs : Ram: 72GB
OS: Redhat EL 5.3 Base Server
COMPILER: Intel C compiler Version 11.0

Lagrangian element is three. As such, the Lagrangian element requires the analysis model to have a greater number of degrees of freedom. Therefore, comparing Cases T4 and Case T8 reveals that the computational time required for the Lagrangian element is 5 times that for the Eulerian element, although the symmetric sparse matrix for the system equations is used for the analysis using the Lagrangian element.

5. Conclusions

In the present paper, a three-dimensional Lagrangian fluid finite element was applied to the seismic response analysis of an oil storage tank with a floating roof, and the obtained results were examined. It was confirmed that, using appropriate parameters for the rotational penalty and the hourglass control as well as the projected mass method, the proposed method can provide sloshing natural frequencies that are consistent with the theoretical solution. Moreover, the transient analysis using the proposed method was shown to provide almost the same results as the strong coupling method for the Eulerian element based on the potential flow theory and the Lagrangian structural element. In the analysis of the oil storage tank with a single-deck floating roof of 80 m in diameter and a liquid level of 20 m, it was shown that the elastic effect of the tank wall on the response was small, and the analysis model considering the free surface was shown to provide almost the same results as the analysis model considering the floating roof. This suggests that the seismic response analysis of the present paper for an oil storage tank with a floating roof does not necessarily require modeling of the floating roof. Although stress analysis of the floating roof is required in order to perform the safety assessment analysis, modeling of the floating roof structure is preferable.

The rotational penalty and the hourglass control parameters used in the proposed method are empirical and may depend on the finite element mesh. However, since the theoretical sloshing natural frequency is known for the cylindrical tank analyzed in the present paper, these parameters can be optimized before transient analysis by comparing the obtained results with the theoretical solution. If the proposed method is applied to more general problems, the theoretical solutions of

which are unknown, the mesh dependence of the numerical solution should be investigated for the eigenvalue analyses before performing transient analyses.

Although the number of degrees of freedom for an Eulerian fluid element based on the potential theory is one, the number of degrees of freedom for the proposed Lagrangian fluid element is three. Therefore, the total number of degrees of freedom of the analyzed model and the computational cost increase. However, the compatibility condition for the displacement between the fluid and the solid can easily be satisfied by using Lagrangian elements, and these elements can be used in the existing finite element code for structural analyses. The coupling analysis using the Lagrangian element provides the system equations with a symmetric sparse matrix, and so the undamped eigenvalue analyses can be easily performed and the modal analyses can be performed in succession. Since the nodal displacements can be approximately expressed using the modal coordinates, the computation time will be reduced.

Acknowledgements

References

Bathe, K.J. (1982), *Finite Element Procedures in Engineering Analysis*, Prentice-Hall.

Belytschko, T., Liu, W.K. and Moran, B. (2000), *Nonlinear Finite Elements for Continua and Structures*, John Wiley & Sons, Ltd.

Belytschko, T. and Bindeman, L.P. (1993), "Assumed strain stabilization of the eight node hexahedral element", *Comput. Meth. Appl. Mech. Eng.*, **105**(2), 225-260.

Calayir, Y. and Dumanoglu, A.A. (1993), "Static and dynamic analysis of fluid and fluid-structure systems by the Lagrangian method", *Comput. Struct.*, **49**(4) , 625-632.

Chen, H.C. and Taylor, R.L. (1990), "Vibration analysis of fluid-solid systems using a finite element displacement formulation", *Numer. Meth. Eng,*, **29**(4), 683-698.

Dogangun, A., Durmus, A. and Ayvaz, Y. (1996), "Static and dynamic analysis of rectangular tanks by using the Lagrangian fluid finite element", *Comput. Struct.*, **59**(3), 547-552.

Fung, Y.C. (1965), *Foundations of Solid Mechanics*, Englewood Cliffs, NJ, USA.

Hamdan, F.H. (1999), "Near-field fluid-structure interaction using Lagrangian fluid finite elements", *Comput. Struct.*, **71**(2), 123-141.

Ibrahim, R.A. (2005), *Liquid Sloshing Dynamics: Theory and Applications*, Cambridge University Press.

Kim, Y.S. and Yun, C.B. (1997), "A spurious free four-node displacement-based fluid element for fluid-structure interaction", *Eng. Struct.*, **19**(8), 665-678.

Koketsu, K., Hatayama, K., Furumura, T., Ikegami, Y. and Akiyama, S. (2005), "Damaging long-period ground motions from the 2003 Mw 8.3 Tokachi-oki, Japan Earthquake", *Seismol. Res. Lett.*, **76**(1), 58-64.

Matsui, T. (2007), "Sloshing in a cylindrical liquid storage tank with a floating roof under seismic excitation", *J. Press. Vess. T. - ASME*, **129**(4), 557-566.

Matsui, T. (2009), "Sloshing in a cylindrical liquid storage tank with a single-deck type floating roof under seismic excitation", *J. Press. Vess. T. - ASME*, **131**(2), 021303, 1-10.

Nagashima, T., Tsukuda, T., Suemasu, H. and Sogabe, K. (2011), "Seismic response analysis methods of an oil storage tank with a floating roof by a strong coupling method", *Eng. Computation.*, **28**(6), 701-716.

Nagashima, T. (2006), "Numerical simulation of the seismic response of a thin-walled cylindrical liquid storage tank", *Proceedings of the 1st International Symposium for Integrated Predictive Simulation System for Earthquake and Tsunami Disaster*, Tokyo, Japan, October.

Nishi, H., Yamada, M., Zama, S., Hatayama, K. and Sekine, K. (2008a), "Experimental study on the sloshing behavior the floating roof using a real tank", *High Pressure Res.*, **46**, 4-17.

Nishi, H., Yamada, M. and Zama, S. (2008b), "Experimental study of floating roof integrity for seismic sloshing under long-period strong ground motion", *Proceedings of the 2nd International Symposium for Integrated Predictive Simulation System for Earthquake and Tsunami Disaster*, Tokyo, Japan, October.

Nishi, H., Yamada, M., Zama, S., Hirokawa, Y., Sekine, K., Misawa, C. and Mikoshiba, T. (2010), "Experimental study on sloshing behavior of floating roofs by using small-scale cylindrical tank", *High Pressure Res.*, **45**(3), 2-10.

Ormeno, M., Larkin, T. and Chouw, N. (2012), "Influence of uplift on liquid storage tanks during earthquakes", *Coulped Syst. Mech. Int. J.*, **1**(4), 311-324.

Parrinello, F. and Borino, G. (2007), "Lagrangian finite element modelling of dam-fluid interaction: Accurate absorbing boundary conditions", *Comput. Struct.*, **85**(11-14), 923-943.

Wilson, E.L. and Khalvati, M. (1983), "Finite elements for the dynamic analysis of fluid-solid systems", *Numer. Meth.*, **19**(11), 1657-1668.

Yoshida, S., Sekine, K. and Mitsuta, T. (2008), "Element analysis for sloshing response of floating roofs in cylindrical storage tanks", *T. Jpn. Soc. Mech. Eng.*, **74**(740), 814-822. http://www.k-net.bosai.go.jp/

CC